Available online at www.sciencedirect.com

SCIENCE DIRECT®

Ocean Modelling 14 (2006) 241–256

Ocean Modelling

www.elsevier.com/locate/ocemod

An analysis of mechanisms for submesoscale vertical motion at ocean fronts

Amala Mahadevan [a,*], Amit Tandon [b]

[a] *Department of Earth Sciences, Boston University, 685 Commonwealth Avenue, Boston, MA 02215, USA*
[b] *Physics Department and SMAST, University of Massachusetts, Dartmouth, 285 Old Westport Road, North Dartmouth, MA 02747, USA*

Received 3 April 2006; received in revised form 25 May 2006; accepted 26 May 2006

Abstract

We analyze model simulations of a wind-forced upper ocean front to understand the generation of near-surface submesoscale, O(1 km), structures with intense vertical motion. The largest vertical velocities are in the downward direction; their maxima are situated at approximately 25 m depth and magnitudes exceed 1 mm/s or 100 m/day. They are correlated with high rates of lateral strain, large relative vorticity and the loss of geostrophic balance. We examine several mechanisms for the formation of submesoscale structure and vertical velocity in the upper ocean. These include: (i) frontogenesis, (ii) frictional effects at fronts, (iii) mixed layer instabilities, (iv) ageostrophic anticyclonic instability, and (v) nonlinear Ekman effects. We assess the role of these mechanisms in generating vertical motion within the nonlinear, three-dimensionally evolving flow field of the nonhydrostatic model. We find that the strong submesoscale down-welling in the model is explained by nonlinear Ekman pumping and is also consistent with the potential vorticity arguments that analogize down-front winds to buoyancy-forcing. Conditions also support the formation of ageostrophic anticyclonic instabilities, but the contribution of these is difficult to assess because the decomposition of the flow into balanced and unbalanced components via semigeostrophic analysis breaks down at O(1) Rossby numbers. Mixed layer instabilities do not dominate the structure, but shear and frontogenesis contribute to the relative vorticity and strain fields that generate ageostrophy.

---

1. Introduction

The mechanisms by which the physical exchange of water and properties is achieved between the actively forced surface layer of the ocean and the relatively quiescent thermocline have posed some long-standing questions in our understanding of the upper ocean. Vertical motion in the upper ocean is instrumental in supplying nutrients to phytoplankton in the sunlit layers, conveying heat, salt and momentum fluxes, and exchanging gases with the atmosphere. But such motion is difficult to observe in the field because vertical velocities are typically three to four orders of magnitude smaller than mesoscale horizontal velocities, which dominate

---

[*] Corresponding author. Tel.: +1 6173535511; fax: +1 6173533290.
E-mail address: amala@bu.edu (A. Mahadevan).

1463-5003/$ - see front matter © 2006 Elsevier Ltd. All rights reserved.
doi:10.1016/j.ocemod.2006.05.006

the energy of the upper ocean. Similarly, models have lacked the resolution and accuracy to produce reliable vertical velocity fields that can support the rates of vertical exchange inferred from tracer observations. For example, estimates of new production (phytoplankton production relying on a fresh, rather than recycled, supply of nutrients) based on oxygen utilization and cycling rates (Platt and Harrison, 1985, Jenkins and Goldman, 1985, Emerson et al., 1997) and helium fluxes (Jenkins, 1988), are much higher in the subtropical gyres than can be accounted for through the physical circulation in global carbon cycle models (Najjar, 1990, Bacastow and Maier-Reimer, 1991, Najjar et al., 1992, Maier-Reimer, 1993). A number of studies, such as McGillicuddy and Robinson (1997) and McGillicuddy et al. (1998), suggest that eddies, which proliferate the ocean, act to pump nutrients to the euphotic zone. However, a basin-wide estimate for the eddy pumping fluxes (Oschlies, 2002, Martin and Pondaven, 2003) shows that eddies, alone, cannot provide the nutrient flux required to sustain the observed levels of productivity in the subtropical gyres. Modeling studies of frontal regions (Levy et al., 2001, Mahadevan and Archer, 2000) suggest that vertical exchange is enhanced at density fronts, which are ubiquitous to the upper ocean. However, it is only through recent developments in numerical modeling, field sampling and analysis, that we are able to resolve frontal processes at the O(1 km) horizontal length scale, referred to here as the *submeso*scale. At this scale, the Rossby and Richardson numbers become O(1) in localized regions, leading to intense ageostrophic secondary circulation and large vertical velocities, as is seen in models that resolve the submesoscale (e.g., Mahadevan, 2006, Capet et al., 2006). These motions are not targeted by most extant mixing parameterization schemes and need to be resolved and understood before their effects can be parameterized in the next generation of global circulation models.

In a preceding paper (Mahadevan, 2006), we described a suite of numerical modeling experiments with a fully nonhydrostatic, three-dimensional, free-surface ocean model used to simulate the evolution of an upper ocean front in a periodic channel setting. The model domain is rectangular in plan view, with periodic boundaries set 48 km apart in the east–west direction, solid boundaries set 96 km apart in the north–south direction, and a flat bottom at a depth of 800 m. A horizontal grid resolution of 0.5 km is used for the flow fields analyzed here, though 1 km and 0.25 km grid resolutions were also used for comparison and presented in Mahadevan (2006). In the vertical, we use a stretched grid spacing varying from 10 m at the surface to 75 m at depth. The domain is initialized with lighter water in the southern half of the upper ocean and denser water to the north, as described in Appendix A. The west-to-east density front is most distinct at the surface and in the mixed layer extending to about 50 m depth, and weakens with depth over the pycnocline which extends to approximately 250 m. As the flow field evolves, the front becomes baroclinically unstable and forms mesoscale meanders. When the model is forced with a westerly wind stress, we observe that submesoscale structures with intense vertical velocities develop in the near surface region (upper 50 m). Down-welling is considerably more intense ($\sim$100 m/day) than up-welling, and is concentrated in narrow bands that are roughly 2 km in width. Though the submesoscale structures are not a nonhydrostatic phenomenon, we prefer to use the nonhydrostatic model for better accuracy. At a depth of 50–100 m, the vertical velocities are weaker ($\sim$10 m/day) and mesoscale in structure. Fig. 1 shows the surface density field and the vertical velocities at two different depths as the flow evolves in time. The front, which is initially straight and oriented west-to-east, develops meanders, which in turn develop more complex submesoscale structure due to the interplay between wind, buoyancy gradients and Coriolis effects. Our objective is to understand the mechanisms that underlie the submesoscale vertical motion seen in the model.

Several mechanisms have been proposed for the development of submesoscale structure in the presence of horizontal density gradients. (i) Horizontal density gradients intensify in the presence of lateral strain and convergence leading to frontogenesis and large vertical velocities (Hoskins and Bretherton, 1972). (ii) Mixing momentum in the presence of horizontal density gradients also generates vertical motion (Garrett and Loder, 1981). (iii) Molemaker et al. (2005) show that ageostrophic anticyclonic baroclinic instability can arise spontaneously at submesoscales in the ocean from a loss of balance in regions where the local Rossby number is large. (iv) Fox-Kemper et al. (2006) propose that mixed layer instabilities (MLI) arise as density fronts that are out of geostrophic balance, slump and re-stratify the upper ocean; these generate submesoscale structure in regions where the Richardson number is small. (v) Thomas and Lee (2005) suggest that along-front winds can generate intense down-welling due to cross-front Ekman transport at the surface. This transport drives dense water over buoyant, resulting in secondary ageostrophic circulation cells that feed back upon themselves and enable exchange with deeper waters.

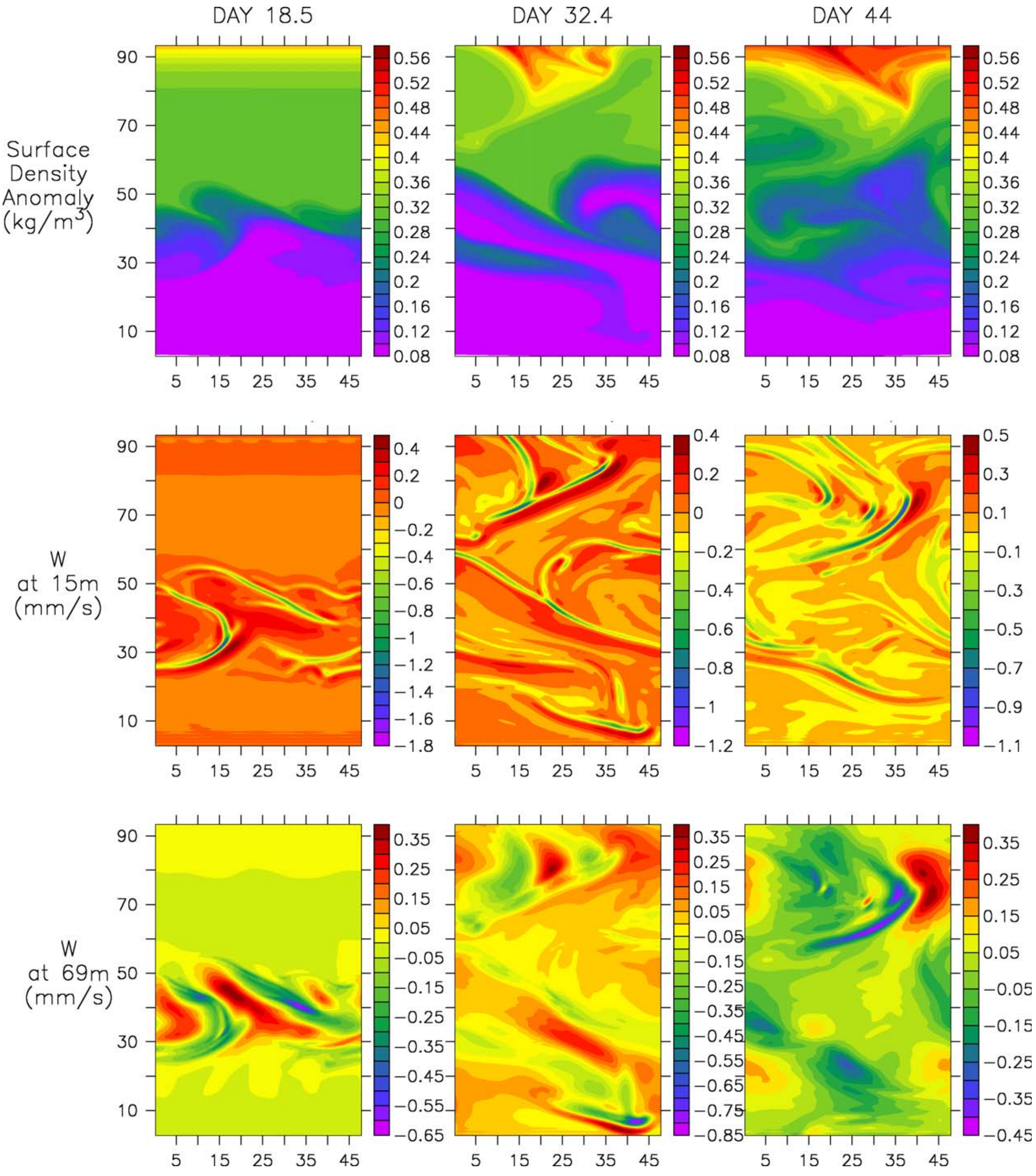

Fig. 1. The density and vertical velocity fields shown in plan view at three different times in the simulation. The top row shows the evolution of surface density, the second row shows the near-surface (15 m depth) vertical velocities and the lowermost row shows the vertical velocities at a depth of 69 m. The color bars indicate the minimum and maximum values in each panel. The structure and intensity of the vertical velocities differ between the near-surface (15 m) and depth (69 m). The domain dimensions are in km. A 4 km wide region adjacent to the solid N and S boundaries is omitted from these and all other figures to eliminate boundary induced up-/down-welling from the picture. (For interpretation of the references in colour in this figure legend, the reader is referred to the web version of this article.)

In the analyses presented here, we test whether the above mechanisms are responsible for generating the submesoscale vertical velocity structure in the model (Fig. 1). These mechanisms have previously been diagnosed in specific settings, some of which are two-dimensional, and analyzed in the linear regime. Here, we use ideas from previous and recent studies to unravel the mechanisms acting three-dimensionally, and in concert, to generate the submesoscale structure seen in the model.

In what follows, we examine several mechanisms that might account for the submesoscale vertical velocities in the model. In Section 2, we examine frontal mechanisms that invoke strain, as well as vertical mixing, to explain up- and down-welling. In Section 3, we estimate the vertical stability of the water column using the Richardson number to determine whether mixed layer instabilities might develop (Fox-Kemper et al., 2006, Stone, 1970). Next, we examine the criteria under which baroclinicity could give rise to submesoscale instabilities (Molemaker et al., 2005). We diagnose the balanced part of the vertical velocity field from the density structure using the omega equation in order to determine whether the submesoscale velocity structure could be ascribed to a loss of balance (McWilliams et al., 2001). In Section 4, we examine forced vertical motion due to the nonlinear Ekman effect (Thomas and Lee, 2005) and analyze the potential vorticity (PV) and PV fluxes to assess the role of wind (Thomas, 2005). We test the scaling for the vertical nonlinear Ekman velocity (Thomas and Rhines, 2002) against the model within a localized region of the model domain. In conclusion, we discuss the combination of effects that lead to the submesoscale structure in the model. We speculate on the implications of such submesoscale activity in the upper ocean and discuss some outstanding questions and future work.

2. Frontal mechanisms

Fronts, or lateral buoyancy gradients, are ubiquitous to the upper ocean (Ullman and Cornillon, 1999), and are sites where large vertical velocities can develop. Due to thermal wind balance, fronts are associated with a surface-intensified jet with strong shear and relative vorticity of opposite sign on either side. Here, we consider two mechanisms that generate vertical motion at fronts. We diagnose their effectiveness and assess whether they account for the submesoscale vertical velocities in the model.

2.1. Strain driven frontogenesis

The first mechanism that we consider is frontogenesis (Hoskins and Bretherton, 1972), or the intensification of fronts due to horizontal strain and convergence in the flow. Strain may be generated by nonlinear dynamics in conjunction with wind forcing. Regions of high strain can be expected to be related to high vorticity due to large shear in the vicinity of high strain rates. The large relative vorticity, which implies large local Rossby number, generates a loss of geostrophic balance and ageostrophic motion. When fluid parcels cross from one side of the front to the other, one can expect a change in the thickness of isopycnal layers due to the conservation of potential vorticity (PV), and hence the development of large vertical velocities (Pollard and Regier, 1990, Pollard and Regier, 1992, Voorhis and Bruce, 1982). This mechanism, by itself, is adiabatic, but can result in diabatic exchange and submesoscale structure when combined with other mechanisms discussed further below.

We examine the relationship between the horizontal strain rate $S \equiv ((u_x - v_y)^2 + (v_x + u_y)^2)^{1/2}$ (where u,v are the velocity components in x, y, i.e., east and north, directions), relative vorticity $\zeta \equiv v_x - u_y$, and submesoscale vertical velocities in the model. In Fig. 2(b) and (c), we plot the near surface vertical velocity field w from the model and the corresponding rate of horizontal strain S (normalized by f) at the same instant of time. We also calculate the relative vorticity ζ and the Rossby number $Ro \equiv \zeta/f$, where f is the planetary vorticity (Fig. 2(d)). The relative vorticity is more cyclonic than anti-cyclonic, as seen in multiple studies of strain-driven frontogenesis e.g., (Hoskins et al., 1978, Thomas and Lee, 2005). Semigeostrophic dynamics can explain the preponderance of cyclonic vorticity. The rate of change of absolute vorticity $A \equiv \zeta + f$, following a fluid parcel is proportional to $-\delta A$, where $\delta \equiv u_x + v_y$ is the divergence. When $Ro \ll 1$, the growth of ζ is dependent only on $-\delta f$ and therefore independent of the sign of ζ. In this case, the growth of cyclonic and anticyclonic vorticity are symmetric. When $Ro \sim 1$, the response is asymmetric. For $|\zeta| < f$, the rate of growth of cyclonic vorticity exceeds that of anticyclonic vorticity of equal magnitude. For $|\zeta| > f$, cyclonic vorticity grows in the presence of convergence ($\delta < 0$), whereas anticyclonic vorticity decays (Bluestein, 1993). Another argument for greater cyclonic vorticity presented in Pedlosky (1987) (cf. Equation 8.4.67) uses the Hoskins and Bretherton (1972) theory and the conservation of vorticity to show that in two-dimensions, the baroclinic generation of

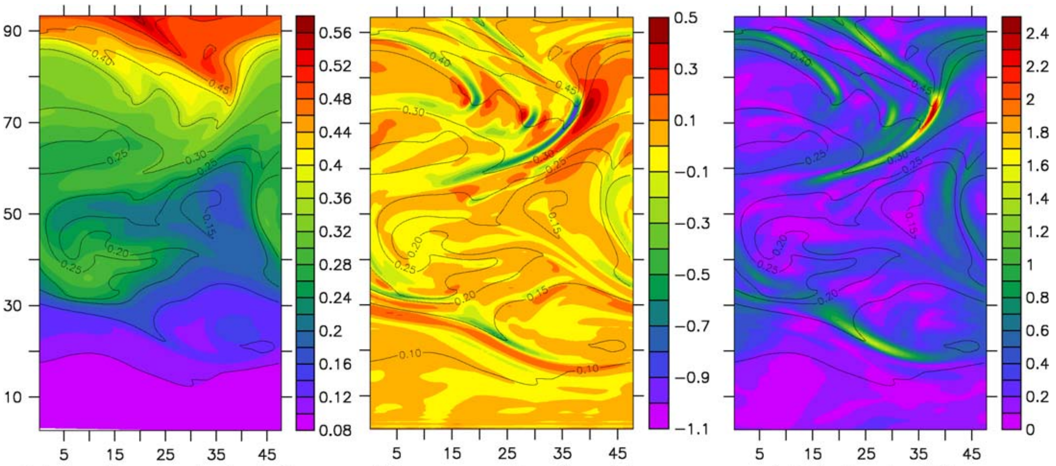

(a) Density anomaly (kg/m^3) (b) w near surface (mm/s) (c) Strain rate S/f

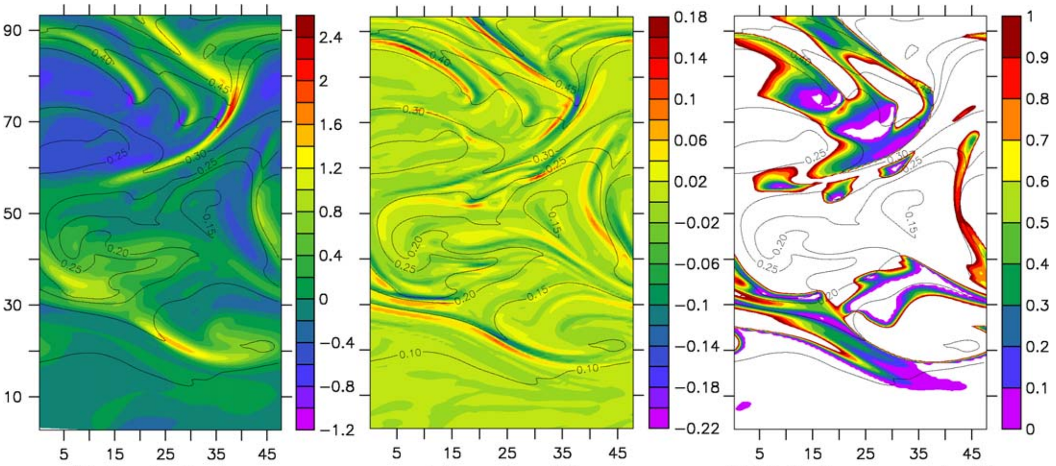

(d) Rossby Number (e) w_{GL} (mm/s) (f) Ri (in the range 0 to 1)

Fig. 2. The near surface fields at 15 m depth from day 44 of the simulation show (a) surface density anomaly, (b) vertical velocity, (c) normalized strain rate S/f, where $S = ((u_x - v_y)^2 + (v_x + u_y)^2)^{1/2}$, (d) local Rossby number calculated as $Ro = \zeta/f$, where negative values indicate anticyclonic relative vorticity, ζ, (e) w_{GL}, an estimate of the vertical velocity due to frictional effects at fronts (Garrett and Loder, 1981), and (f) Richardson number $Ri = N^2/((\partial u/\partial z)^2 + (\partial v/\partial z)^2)$ in the range 0–1 (higher values are not plotted).

vorticity must be zero to lowest order. Consequently, vorticity would be proportional to the local Richardson number Ri, and hence positive.

The correspondence between w, S and Ro in Fig. 2(b)–(d) suggest that high strain is associated with large relative vorticity and regions of high cyclonic vorticity are associated with intense down-welling. Sectional views in Fig. 3(a)–(b) show that while the broader up-/down-welling structure at the 50 m depth (at $x = 36$ and 42 km) is associated with the mesoscale, the intense down-welling at 20–25 m depth (at $x = 30$ and 37 km) is at submesocales. The submesoscale down-welling occurs near regions of high strain that have surface maxima (Fig. 3(c)), but the down-welling velocity maxima are shifted at depth with respect to the sites of maximum strain. These are regions of large convergence $-\delta$, in which $-\delta$ amplifies the cyclonic relative vorticity ζ, resulting in large, positive Ro (Fig. 3(d)). In this regime, quasigeostrophic (QG) scaling is not valid as Ro is not small and isopycnals outcrop. Therefore, semigeostrophic (SG) scaling is more appropriate. SG theory also suggests more rapid intensification of frontal gradients than QG theory. However, we show later that the existing framework for predicting vertical velocities using SG theory breaks down at submesoscales since there are regions in the domain where the PV changes sign or $Ro = -1$, as seen, for example, in Fig. 3(d).

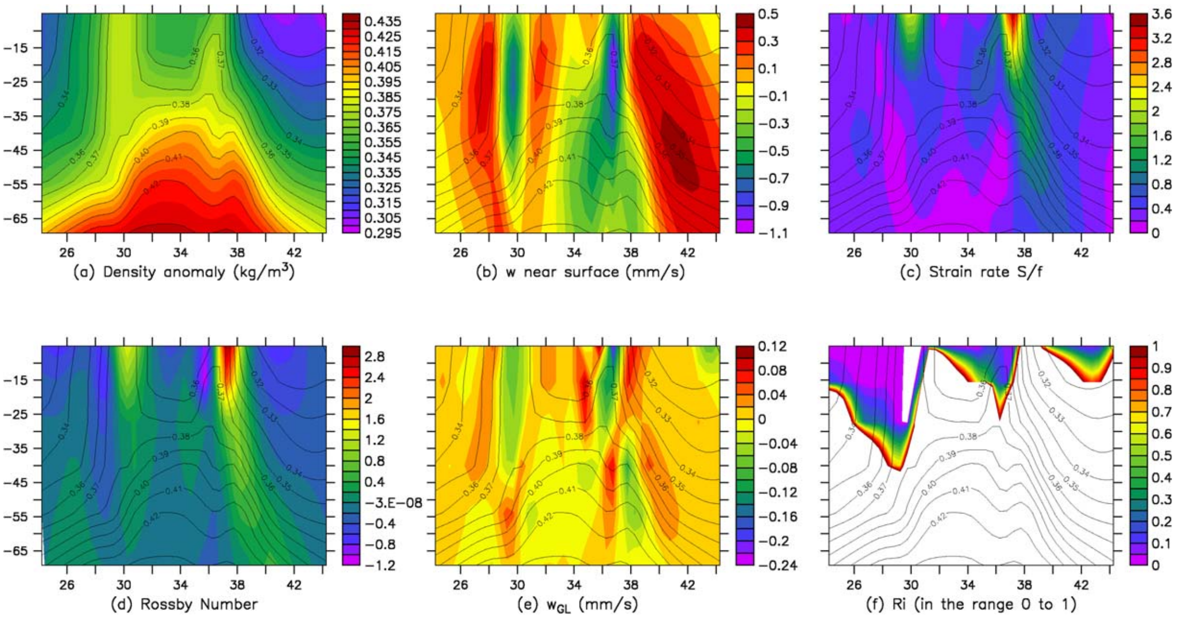

Fig. 3. A west-to-east vertical section at $y = 72$ km, extending from $x = 24$ to 44 km and $z = 0$ to 70 m depth, showing the same variables as in Fig. 2, namely, (a) density anomaly, (b) model vertical velocity, (c) normalized strain rate S/f, (d) Ro, (e) w_{GL}, and (f) Ri in the range 0–1. Regions of intense down-welling are not well correlated with small Ri, but are where S is large, and Ro is large and changing from negative to positive. Ro, however, does not account for the transverse contributions to vorticity, which are also significant, as shown later.

2.2. Frictional effects at fronts

The next mechanism that we consider, generates vertical velocity from the divergence of the cross frontal flow in the presence of frictional effects without wind forcing. This mechanism assumes that the across-front pressure gradient is in geostrophic balance with the along-front Coriolis acceleration, but there is no pressure gradient in the along-front direction. The across front Coriolis acceleration is thus balanced by vertical mixing of momentum in the limit of small Rossby and Ekman number, i.e., $fv \sim \partial(A_{\mathrm{V}}\partial u/\partial z)/\partial z$ (Garrett and Loder, 1981, Thompson, 2000). Here u, v are along- and cross-frontal velocity components, respectively, f is the Coriolis parameter, and A_{V} is the vertical eddy viscosity. Defining the buoyancy b, in terms of the density variation ρ', and mean density ρ_0, as $b \equiv -g\rho'/\rho_0$, and using thermal wind balance $\partial u/\partial z = f^{-1}\partial b/\partial y$ (where y is the cross-frontal direction) to eliminate $\partial u/\partial z$ from the frictional term, Garrett and Loder (1981) integrate the divergence of the cross-frontal velocity v, to deduce that the vertical velocity scales as

$$w_{\mathrm{GL}} \sim -\frac{1}{f^2}\frac{\partial}{\partial n}\left(A_{\mathrm{V}}\frac{\partial b}{\partial n}\right). \tag{1}$$

Here, n is used in place of y to denote the direction of the horizontal buoyancy gradient so as to make the relationship generalizable to fronts that are changing in orientation. The subscript GL refers to Garrett and Loder (1981). For an x, y gridded density field, b_{nn} can be calculated using $b_{nn} = b_{xx} + b_{yy} + b_{xy}\left(\frac{b_x}{b_y} + \frac{b_y}{b_x}\right)$, where $b_{nn} = b_{xx}$ if $b_y \to 0$ and $b_{nn} = b_{yy}$ if $b_x \to 0$ (c.f. Appendix 1, Tandon and Zhao, 2004). In order to estimate w_{GL} from (1) for our model fields, we use a constant value of $A_{\mathrm{V}} = 10^{-5}\ \mathrm{m}^2\,\mathrm{s}^{-1}$. While this is the value of A_{V} used in the numerical model, it does not take into account the mixing performed through convective adjustment, which was used in all the model runs. Fig. 2(e) shows the value of w_{GL} calculated in this way with the model fields. The pattern of w_{GL} resembles that of w, particularly for down-welling, but the magnitude does not match. In sectional view (Fig. 3(b) and (e)), w_{GL} and w diverge significantly at depth. This is because the theory is simplistic and only linear. Furthermore, the effective value of A_{V} may be higher in the numerical model due to convective adjustment. When the value of A_{V} is adjusted for mixing, however, the estimate for w_{GL} is not closer to w.

3. Spontaneous instabilities

3.1. Mixed layer instability

Horizontal buoyancy gradients in the upper ocean store available potential energy. Fox-Kemper et al. (2006) discuss how this energy in the mixed layer is released by an unforced mixed layer instability (MLI) that affects the restratification process as an unbalanced front slumps. Its characteristic vertical scale is the depth of the mixed layer, typical horizontal scales are a few kilometers, and growth rates are of the order of a day. Therefore, it is relevant to the development of submesoscale structure. In unstable regions, the local Richardson number Ri, satisfies the relationship $Ro^2 Ri \sim 1$. Fox-Kemper et al. (2006) assume an idealized basic state as a zero-PV initial state that becomes unstable at low, O(1) Ri and large, O(1) Ro. This is in contrast to small Ro baroclinic instability, where the vertical scale is the depth of the thermocline, typical horizontal scales are ~10–100 km, $Ri \gg 1$, and $Ro \ll 1$.

In our numerical simulations, we marginally resolve the wavelength k and the time scale associated with the growth rate σ_i, governing the most unstable mode in the instability mechanism described by Stone (1970). This forms the basis of MLI (Fox-Kemper et al., 2006); k and σ_i are given by $k = \frac{u_0}{f}\left(\frac{5/2}{1+Ri}\right)^{\frac{1}{2}}$ m, where u_0 is the along-front velocity (in m s^{-1}) generated from thermal wind balance and f is in s^{-1}; $\sigma_i = f\left(\frac{5/54}{1+Ri}\right)^{\frac{1}{2}} S^{-1}$. For example, the wavelength of the most unstable mode is approximately 1 km for $Ri = 2, f = 10^{-4}$ s^{-1} and a characteristic horizontal velocity of 0.1 m s^{-1}; our horizontal grid resolution of 500 m would marginally resolve this. For a short duration, we ran the model at a horizontal grid resolution of 250 m by interpolating the developed flow fields from the 500 m resolution model run as initial conditions. We did not find striking differences between results of the 250 m and 500 m resolution runs (c.f. Fig. 6 Mahadevan, 2006). The e-folding time scale for growth of the most unstable mode is approximately half a day and is well resolved by the model, which uses a time step of 400 s. To test whether MLI contributes to the submesoscale structure observed in our simulations, we estimate the Richardson number $Ri \equiv N^2/(\partial u/\partial z)^2$, for the model flow fields (see Figs. 2(f) and 3(f)). The correspondence between regions of small Ri and high vertical velocity is too weak to support the idea that instabilities associated with low Ri are the cause of the intense vertical submesoscale motion seen in the model. The finite amplitude version of MLI may differ substantially from the linear case (B. Fox-Kemper, personal communication (2006)), but if MLI does occur in our numerical simulations, it likely plays only a minor role. This is because we initialize the model with a geostrophically balanced state and force the surface continually with a wind stress. A larger model domain that allows for the interaction between submesoscales and mesoscale eddies and uses geostrophically unbalanced initial conditions would be conducive to MLI, as shown by B. Fox-Kemper (AGU, Ocean Sciences, 2006). In our model, we see the early development of MLI when using higher (250 m) grid resolution and no wind forcing.

3.2. Loss of balance and ageostrophic anticyclonic baroclinic instability

McWilliams et al. (2001) review three main routes to dissipation of energy from a balanced flow through the loss of balance. The conditions for all three of these are satisfied in our simulations. They are: (i) change in sign of the absolute vorticity A, which gives rise to symmetric centrifugal instability[1], (ii) change in sign of the vertical buoyancy gradient or N, which gives rise to convection, and (iii) change in sign of the difference between absolute vorticity and strain rate A–S, which gives rise to a new class of unbalanced ageostrophic instabilities (Molemaker et al., 2005, McWilliams, 2003) that may explain the genesis of submesoscale motion. This class of instabilities has been investigated for a frontal situation by Molemaker et al. (2005), for a boundary current by McWilliams et al. (2004), and for a Taylor-Couette flow by Molemaker et al. (2001). For the frontal initial state, the dynamics of hydrostatic and thermal-wind balance gives way to ageostrophic baroclinic instabilities at length scales of 0.1–10 km. Significant ageostrophic modes arise for Ro between 0 and 1 (e.g., for $Ro = 1/\sqrt{2}$, or $Ri = 2$) from a simple initial state of uniformly sheared parallel flow (Molemaker

---

[1] A more general condition for symmetric instability is the change in sign of the Ertel PV.

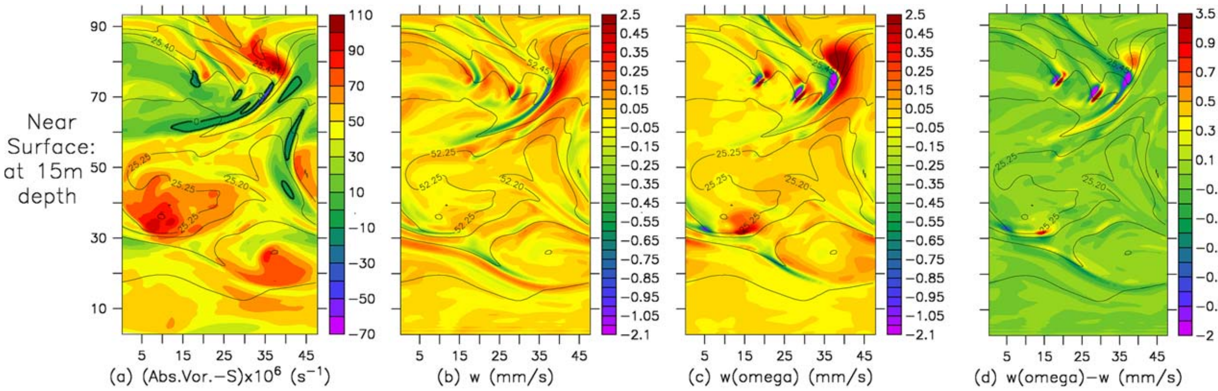

(a) (Abs.Vor.−S)x10^6 (s^{-1}) (b) w (mm/s) (c) w(omega) (mm/s) (d) w(omega)−w (mm/s)

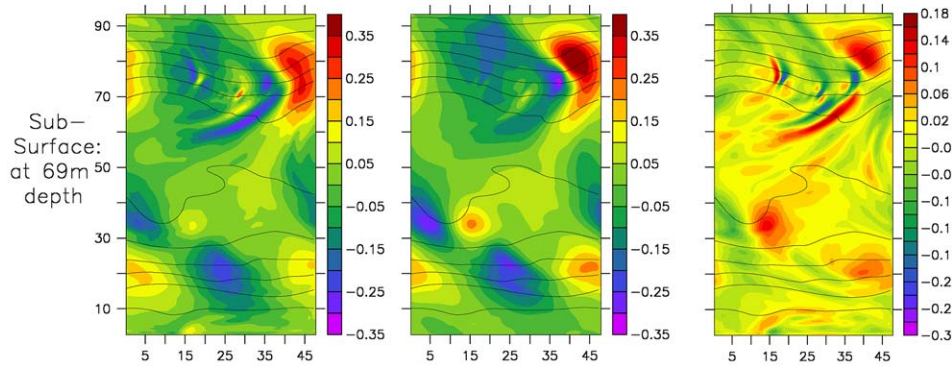

(e) w (mm/s) (f) w(omega) (mm/s) (g) w(omega)−w (mm/s)

Fig. 4. An analysis of the model flow fields from day 44 to assess whether conditions are favorable for the growth of ageostrophic anticyclonic instabilities. All plots are overlaid with thin black contours corresponding to density from the same depth. (a) Difference between the absolute and relative vorticity, A–S, at 15 m. The thick black contour marks the zero-crossover, where ageostrophic anticyclonic instabilities are expected to develop (Molemaker et al., 2005). Figs. (b)–(d) show (at a depth of 15 m) the model vertical velocity w, the vertical velocity w^{Ω}, computed from the density field using the QG omega equation representing balanced dynamics, and the difference $w^{\Omega} - w$. The non-uniform spacing at the ends of the color key in (b)–(d) is chosen to accommodate the extreme values in w^{Ω} generated by the omega equation. The maximum and minimum values of w in (b) do not utilize the extremes in the color key. Figs. (e)–(g) show the same at a depth of 69 m. Note the asymmetry and larger range in the color bars of (b)–(d) as compared to (e)–(f). (For interpretation of the references in colour in this figure legend, the reader is referred to the web version of this article.)

et al., 2005). To test where such as loss of balance occurs and whether these instabilities play a role in setting up the submesoscale structure observed in our simulations, we plot A–S from the model fields and look for coincidence between the zero crossings of A–S and regions of intense up-and down-welling (Figs. 4(a) and (b)). A–S remains largely positive, but changes sign within narrow regions. The region where A–S changes sign most prominently, is coincident with the most intense down-welling site in the domain, suggesting that conditions are appropriate for the loss of balance conditions and the development of ageostrophic anticyclonic instability.

3.3. Quasigeostrophic balanced analysis using the omega equation

To assess whether the submesoscale structure in the model arises from a loss of balance, we attempt to differentiate between the component of the vertical velocity field that results from balanced dynamics, and the part that may be ascribed to a loss of balance. This decomposition of the fields into balanced and unbalanced components is done by using the solution of the quasigeostrophic (QG) omega equation (Hoskins et al., 1978) as a representation of balanced dynamics. We find the geostrophic velocity $\mathbf{u}_g$, using the hydrography from the model and numerically solve the three-dimensional, elliptic QG omega equation (Rudnick, 1996, Shearman et al., 1999), namely,

$$\nabla_h^2(N^2 w^\Omega) - f_0^2 \frac{\partial^2 w^\Omega}{\partial z^2} = \nabla_{\mathbf{h}} \cdot \mathbf{Q}, \quad \text{where} \quad \mathbf{Q} = 2\frac{g}{\rho_0}\left(\frac{\partial \mathbf{u}_g}{\partial x} \cdot \nabla_{\mathbf{h}}\rho, \frac{\partial \mathbf{u}_g}{\partial y} \cdot \nabla_{\mathbf{h}}\rho\right), \tag{2}$$

to diagnose the balanced component of the vertical velocity w^Ω. The boundary conditions are taken to be $w^\Omega = 0$ at the boundaries, with an appropriate level of no motion chosen for the lower boundary. The resulting w^Ω is compared to the vertical velocity w from the model. Large differences are seen between w^Ω and w in the near-surface (Fig. 4(b)–(d)), but w^Ω resembles w much better at a depth of 69 m (Fig. 4(e)–(g)). Hence the QG omega equation is able to explain the mesoscale vertical motion at depth (50–100 m), but not the submesoscale motions closer to the surface (0–50 m). The lack of correspondence between w^Ω and w in the near-surface suggests that unbalanced dynamics and ageostrophic anticyclonic instabilities may have a role in the submesoscale up- and down-welling observed in the model. Also, frictional effects near the surface are clearly important and not represented in the QG omega equation.

Since the QG omega equation is based on the lowest order QG approximation and does not allow variations in stratification, one may ascribe its failure in the near-surface layer to the lack of additional advective terms and restrictions on stratification that are relaxed in the semigeostrophic (SG) form of the omega equation. In order to attempt a higher order decomposition of the field, we considered two approaches to solving the SG omega equation. The first, described by Pinot et al. (1996) following Hoskins et al. (1978), requires interpolating the model variables into a geostrophic coordinate system. For our highly nonlinear simulations, a non-monotonic mapping between the model variables and geostrophic coordinates arises in regions of submesoscale activity. This prevents the interpolation onto geostrophic coordinates, unless the submesoscale features are smoothed out. The second approach suggested by Viúdez and Dritschel (2004), solves the SG equations directly but requires a coordinate mapping via a Jacobian operator, which becomes singular in regions where $Ro \to -1$ or $A \to 0$ (Fig. 3(d)). The separation into balanced and unbalanced dynamics thus breaks down with these approaches in the semigeostrophic case, since our domain includes regions where A changes sign.

4. Forced motion: Ekman pumping by down-front winds

The nonlinear Ekman transport induced normal to the wind stress τ, acting at the surface is given by $M_E = -\tau\rho^{-1}\,(f+\zeta)^{-1}$ (Stern, 1965, Niiler, 1965, Thomas and Rhines, 2002), assuming a two-dimensional and steady setting. In a plane normal to the wind stress, ζ takes on the definition $\zeta = -\partial u_\tau/\partial n$, where u_τ denotes the velocity parallel to τ, and n is oriented at $+\pi/2$ with respect to τ. When the Rossby number is O(1), the resulting Ekman transport differs significantly from the traditional formulation in which ζ is neglected. The Ekman pumping velocity that results from taking ζ into account is given (e.g., Thomas and Rhines, 2002) by

$$w_E = \frac{-1}{\rho A}\frac{\partial \tau}{\partial n} + \frac{\tau}{\rho A^2}\frac{\partial \zeta}{\partial n}, \tag{3}$$

where $A = \zeta + f$. When a wind acts on a region where lateral buoyancy gradients $\nabla_h b$ exist at the surface, the along-front component of the wind stress τ, which is normal to $\nabla_h b$ and n, generates an Ekman pumping velocity w_E that leads to the intensification of ageostrophic secondary circulation cells at the front (Thomas and Lee, 2005). When the wind stress is spatially uniform, the first term in (3) does not come into play. Lee et al. (1994) and Klein and Hua (1988) have examined the nonlinear Ekman effect in a a two-dimensional setting with uniform τ. Using linear stability analysis, Thomas and Lee (2005) identified the most unstable modes of the ageostrophic secondary circulation and found them to be quasi-stationary. We compare the intense near-surface vertical velocities w, in the model with the scaling for the nonlinear Ekman pumping velocity in (3) to test whether the model w is generated by nonlinear Ekman pumping. Fig. 5 shows the one-dimensional frontal diagnosis of w_E along the locally cross-front section shown in Fig. 5(a). We take the section normal to the front in the region of most intense w, and using the horizontal velocities from the model, calculate ζ and $\frac{\partial \zeta}{\partial n}$. Since the model uses a constant, uniform westerly wind stress, only the second term in (3) is considered. The strong lateral density gradients at approximate local coordinates of 0 km and 7 km in the figure, give rise to large variations in the along-front surface velocity and sharp increases in cyclonic

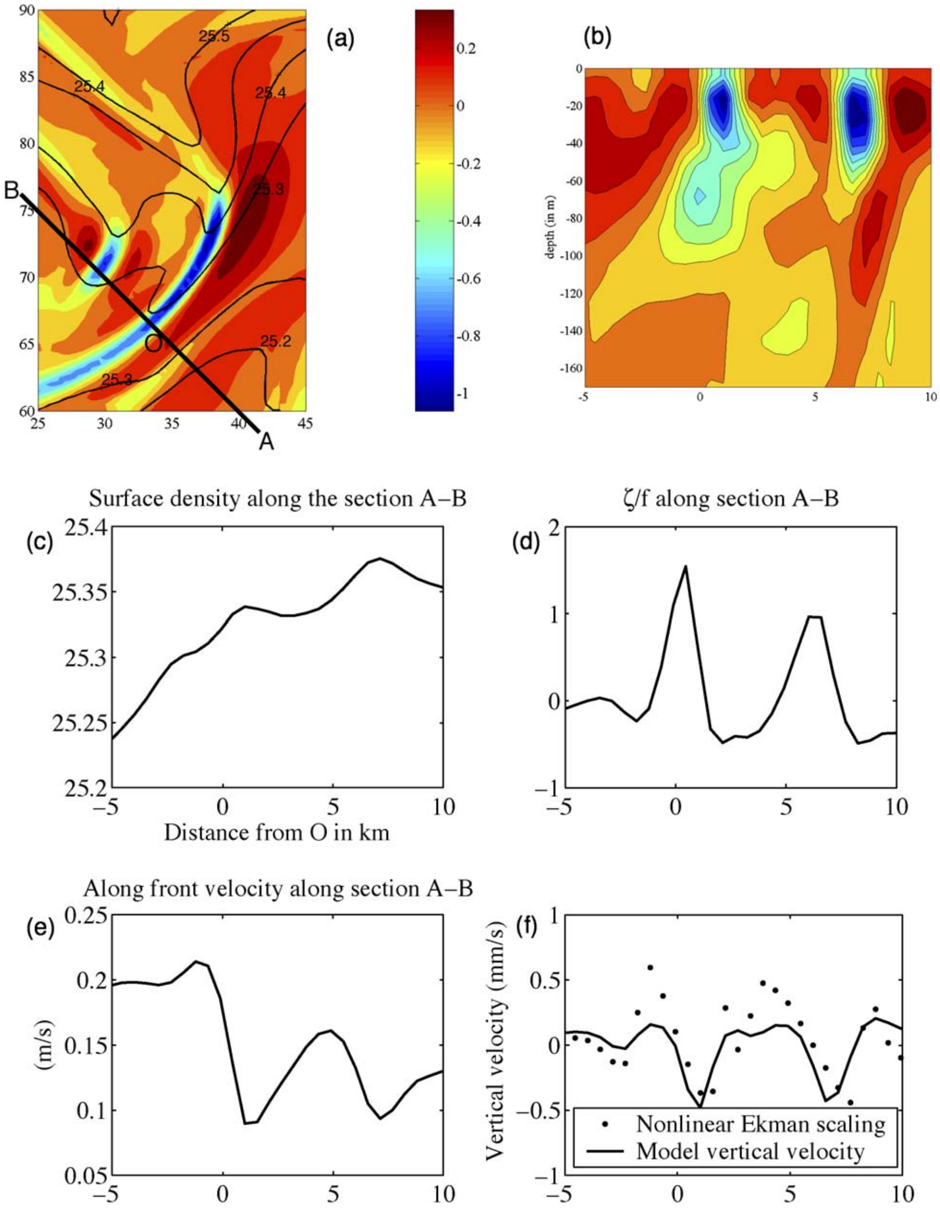

Fig. 5. A one-dimensional diagnosis of the nonlinear Ekman pumping velocity evaluated along the section A–B oriented south-east to north–west (at 135°), so as to be locally normal to the front on day 44 of the model simulation. (a) The vertical velocity field from within a subregion of the model shown in plan view at a depth of 15 m. (b) Vertical velocities along section A–B showing the near-surface submesoscale maxima and deeper mesoscale structures. (c) Density, (d) ζ/f, and (e) horizontal velocity normal to section A–B, shown along A–B at a depth of 8 m. In (f), we show model vertical velocity (solid) and the Ekman pumping velocity (dots) derived from Eq. (3) at 8 m depth, with the south-westerly component of wind stress τ, normal to section A–B, and the differentiation of ζ along section A–B. Here, $\zeta = -\partial u_\tau/\partial n$, where n is oriented along A–B and u_τ is the velocity in the direction oriented at $+\pi/2$ with respect to n. The magnitude and location of down-welling are diagnosed well by the Ekman pumping velocity relationship, but up-welling is predicted to be just as large as down-welling, unlike the case in the model.

relative vorticity that result in O(1)Ro (Figs. 5(c)–(e)). Positive and negative across-front gradients of ζ result in negative and positive w_E, respectively. The estimate for negative w_E (down-welling) obtained from scaling in (3) is well-matched with the model w in location and magnitude (Fig. 5(f)). Positive values of estimated w_E are highly exaggerated compared to the model. The large asymmetry in the magnitude of up- and down-welling seen in the model is thus not captured by the simple scaling. In this instance, the vorticity increase is sharper on the buoyant side of the front and counter balances the decrease in w_E's magnitude due to the increase in A. Moreover, this scaling is two-dimensional and steady, and clearly does not apply when A approaches zero.

Another view of the same mechanism is presented by Thomas (2005) in terms of the Ertel PV, henceforth $\text{EPV} \equiv \boldsymbol{\omega}_\mathbf{a} \cdot \nabla b$, where $\boldsymbol{\omega}_\mathbf{a} \equiv (w_y - v_z, u_z - w_x, f + v_x - u_y)$ is the absolute vorticity vector and $\nabla b = (b_x, b_y, b_z)$ is the gradient of buoyancy in three dimensions. When a front is forced with wind blowing in the direction of the frontal jet, a non-advective frictional EPV flux is induced at the sea surface, extracting EPV from the surface in a manner analogous to buoyancy forcing. Since the isopycnal surfaces are impermeable to EPV

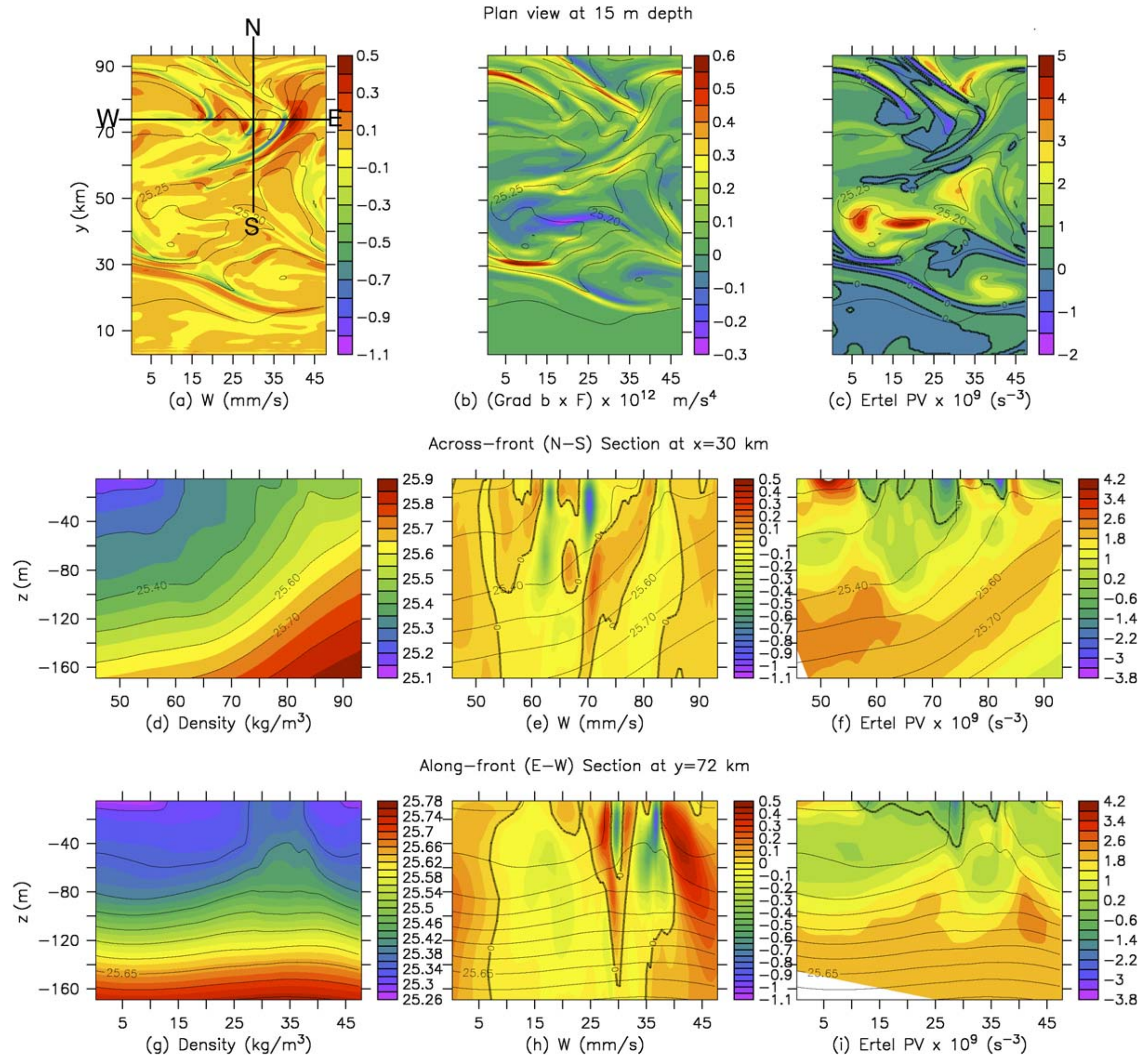

Fig. 6. An evaluation of the correspondence between vertical velocity, the sink for Ertel PV due to nonlinear Ekman effects $\nabla_\mathbf{h} b \times \mathbf{F}$, and Ertel PV. Top row: Plan views at 15 m depth from day 44 of the simulation showing (a) vertical velocity, (b) surface EPV flux $\nabla_\mathbf{h} b \times \mathbf{F}$, where positive means leaving the surface, and (c) Ertel PV. The light contours indicate near-surface density, the dark contour, wherever shown, is the 0 contour for the field shown in color. There is a correlation between regions of negative Ertel PV in (c) and the frictional flux of EPV in (b). Positive values of $\nabla_\mathbf{h} b \times \mathbf{F}$ in (b) indicate where Ertel PV is fluxed out of the surface and correspond loosely with intense down-welling or subduction of low EPV. The middle row of figures (d)–(f) show a south–north section S–N at $x = 30$ km through the upper 165 m. Ertel PV is largely positive in the interior, but low PV water is subducted from the surface by the intense down-welling. The lower row (g)–(i) shows a west–east vertical section W–E. The extreme values of EPV occur at the surface, where wind forcing provides a source/sink for EPV.

(Haynes and McIntyre, 1987), the extraction of EPV at the surface is accompanied by the subduction of low EPV water and the resupply of EPV to the down-welling region through lateral convergence of fluid at the surface. In the process, secondary circulations that scale as the surface frictional flux are set up, conveying an advective EPV flux. The vertical component of the frictional EPV flux at the surface is given by $\nabla_{\mathbf{h}} b \times \mathbf{F}$ (Thomas, 2005), where $\mathbf{F} = \partial_z(A_V \partial u/\partial z)$, $\partial_z(A_V \partial v/\partial z)$ is the non-conservative right hand side of the momentum equation, and is significant due to wind forcing. At the surface, $z = 0$, $A_V \partial(u,v)/\partial z = (\tau^x,\tau^y)$, where τ^x, τ^y are wind stress components acting in x and y directions. At the base of the Ekman layer $z = -\delta_E$, we assume that $A_V \partial(u,v)/\partial z$ is negligible in comparison to the surface, and hence $\mathbf{F}$ can be approximated as $\mathbf{F} = (F^x,F^y) = (\tau^x,\tau^y)/(\rho_0\delta_E)$. We take δ_E to be the turbulent Ekman layer depth, which is approximated as $\delta_E = 0.4u^*/f$, where $u^* = (\tau/\rho_0)^{1/2}$. In our case, $\tau^x = 0.025\ \mathrm{N\,m^{-2}}$, and $\delta_E = 20$ m.

To test whether wind is fluxing EPV out of the surface in the model, we compute the EPV and the vertical component of the frictional EPV flux $\nabla_{\mathbf{h}} b \times \mathbf{F}$. Fig. 6 shows the correspondence between the submesoscale near-surface vertical velocities and the EPV in plan and sectional view. Regions of down-welling correspond to regions of negative EPV, while regions of up-welling correspond to positive EPV. There is also a correlation between low, i.e., O(1) or smaller, values of *Ri* in Fig. 2(f) and EPV in Fig. 6(c), suggesting that EPV is lost in regions of active mixing, which in the model, is performed through convective adjustment.

Forcing at the surface can drive EPV in or out of the surface depending on the sign of $\nabla_{\mathbf{h}} b \times \mathbf{F}$. In regions where $\nabla_{\mathbf{h}} b \times \mathbf{F}$ is positive (Fig. 6(b)), EPV is lost at the surface and negative EPV water is advected downward (Fig. 6(a) and (c)). From the figures, we see that regions of positive $\nabla_{\mathbf{h}} b \times \mathbf{F}$ correspond to negative w (although, not at the site of most intense down-welling) and a loss of EPV from the surface. This corroborates the idea that wind removes EPV from the surface in a manner analogous to buoyancy forcing (Thomas, 2005). The north–south section (Fig. 6(d)–(f)) shows that low EPV water subducts southward between density anom-

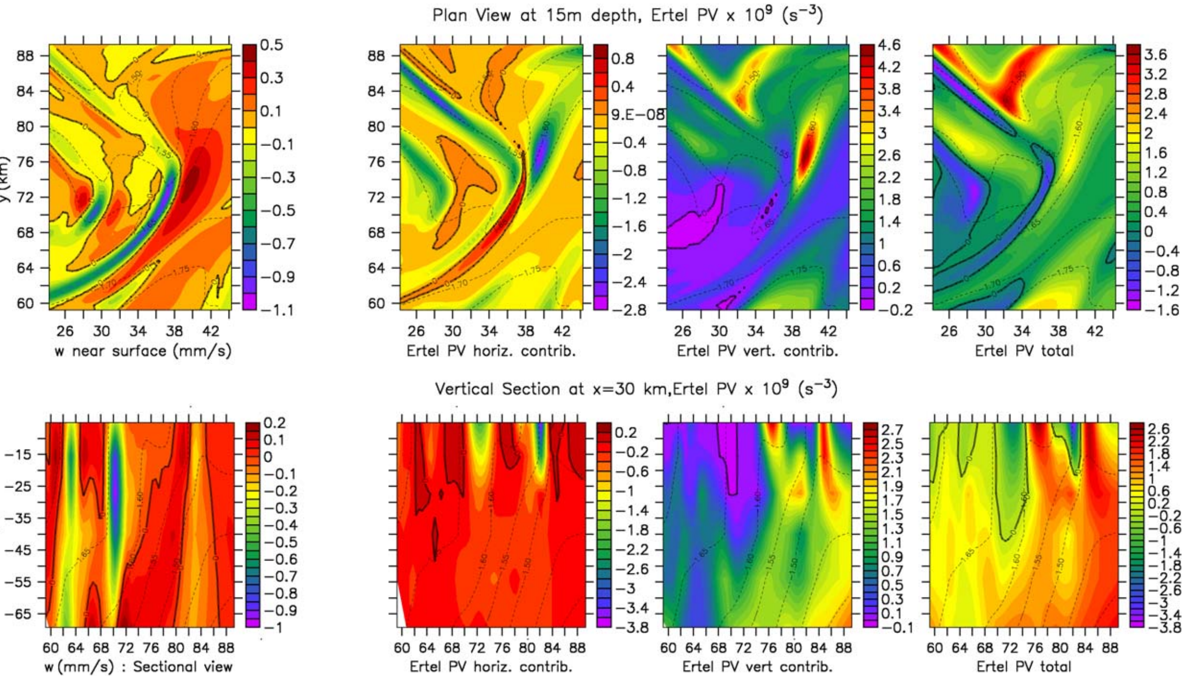

Fig. 7. Top row: Plan views at 15 m depth, and lower row: South to north (along S–N in previous figure) sectional views at $x = 30$ km, showing the model vertical velocity, Ertel PV (EPV), and horizontal and vertical contributions to EPV, from within a sub-region of the model domain shown in earlier figures. The light, dotted contour lines represent the density distribution, the solid dark lines are the zero contour of the field shown in color. The vertical contribution to EPV comprising $(f + \zeta)b_z$, is largely positive, whereas the horizontal contribution $(w_y - v_z)b_x + (u_z - w_x)b_y$, is largely negative. Thus, the near-surface negative EPV that is subducted by intense down-welling, arises from lateral buoyancy gradients (b_x, b_y) and wind-induced vertical shear (u_z, v_z) in the near surface layer. (For interpretation of the references in colour in this figure legend, the reader is referred to the web version of this article.)

aly values of 25.3 and 25.4 reaching ~60 m depth at $x = 72$ km. This is also seen in the east–west section. Fig. 6(g)–(i) show a bolus of low EPV water subducted by the intense submesoscale features, and carried further downward by the deeper down-welling that is characteristic of mesoscale meanders (and is well described by QG dynamics). Temporal variations in EPV are neglected from these analyses.

To further ascertain the contribution to negative EPV near the surface, we plot the horizontal and vertical contributions to the EPV in plan and sectional views alongside the vertical velocity (Fig. 7). The EPV contribution from the vertical component of vorticity, $(f + \zeta)b_z$ is largely positive with small negative components near the surface. The contribution from $(w_y - v_z)b_x + (u_z - w_x)b_y$, is largely negative, with small positive components near the surface. The largest negative contribution to the EPV arises from the horizontal buoyancy gradients and vertical shear in the flow and is maximum at the surface where wind generated shear and lateral buoyancy gradients are most intense. This creates negative EPV at the surface, which can be subducted by intense submesoscale velocities.

5. Summary and discussion

Submesoscales have received relatively little attention until recently because they are notoriously difficult to observe and model. Their presence has become evident through high frequency sampling from towed instrument platforms, high resolution measurements of fluorescence and temperature, high resolution modeling, and theoretical studies such as those cited above. In this paper, we have analyzed the near-surface submesoscale structure and intense vertical velocities that emerge in a three-dimensional, nonhydrostatic model of an upper ocean front forced with down-front winds.

Several candidate mechanisms that can generate vertical motion or submesoscale structure are examined. In three-dimensions, we find that a combination of the mechanisms is necessary to explain the submesoscale structure seen in the model. Baroclinic instability leads to meanders, meanders lead to regions of strain and vorticity; strain generates vertical motion by frontogenesis, vorticity generates non-linear feedback via the Ekman effect which relies on friction and wind forcing to intensify up- and down-welling. Within submesoscale regions the flow field also satisfies the conditions for loss of balance that make a forward energy cascade possible.

The features that develop in our wind-forced model simulations at a horizontal grid resolution of 500 m are finer in scale and different in character from the frontal up- and down-welling described in the modeling study of Levy et al. (2001) using a horizontal grid resolution of 2 km. In the our model, wind plays a critical role in inducing submesoscale structure. The model domain is not large enough to allow the formation and interaction of multiple eddies, which would lead to a more developed strain field. It is conceivable that in such situations submesoscale structure might emerge through some of the mechanisms addressed here, even when wind is weak or absent. Processes such as frontal adjustment are also known to generate submesoscales (Fox-Kemper et al., 2006). Based on our analyses, it seems that the submesoscale structure in the model's flow is dominated by wind. MLI and AAI are thought not to be as dominant, most likely due to the overpowering effect of wind forcing. Conditions in the developed flow field support the generation of AAI, but not MLI. However, we lack a systematic way of identifying the developed forms of AAI and MLI and may be glossing over them as a result.

Thomas and Lee (2005) show that the semigeostrophic Eliassen-Sawyer operator changes character from elliptic to hyperbolic as the EPV changes sign from positive to negative. The hyperbolic nature of the solution allows secondary circulation cells, with sub-surface maxima. The elliptic solutions decay away from the boundary. In the hyperbolic region, the solution to the linear stability problem is non-unique, and any of an infinite number of unstable wavenumbers can be selected. The surface boundary condition on vertical velocity or surface vorticity picks out the scale and the growth rate of the mode for areas with positive EPV, whereas the nonlinear evolution selects the scale for hyperbolic cases, as seen in the the two-dimensional nonhydrostatic simulations of Thomas and Lee (2005). Additionally, in the two-dimensional case, the basic state considered has either positive EPV or negative EPV throughout the mixed layer, and the nature of the mathematical operator remains the same.

In the three dimensional simulations considered here, the situation is more complex. EPV does not have the same sign throughout the region, so the nature of the operator changes from elliptic to hyperbolic in isolated regions in both the horizontal and vertical. Mathematically, the local quasi-2d SG operator becomes singular when the EPV is zero, though it is well behaved with either sign. The SG approximation therefore breaks down, as mentioned earlier.

We can still understand the solutions in the quasi-2d sense if we align ourselves locally with the along-frontal and across frontal direction. The down-welling regions are the regions of negative EPV (Fig. 7), and the quasi-2d SG operator is hyperbolic in these regions, i.e., secondary cells with sub-surface velocity maxima appear, as expected. The up-welling regions in the solutions turn out to be regions with positive EPV (Fig. 7), and the quasi-2d SG operator is elliptic there, i.e., the vertical velocity decays as depth increases. The hyperbolic nature of negative EPV regions necessitates that down-welling is stronger than up-welling, which is associated with regions of elliptic character that are also broader.

It is interesting that the up-/down-welling features that are characteristically associated with mesoscales (deeper than 50 m in our simulations) can link with the intense down-welling zones generated at submesoscales (see Fig. 5(b)), providing an advective path for subduction of low EPV water into the relatively quiescent deeper waters. Further analyses are needed to quantify the net effect of submesoscale to mesoscale coupling on the vertical transport of tracers and nutrients.

Since lateral buoyancy gradients and wind are ubiquitous to the oceans, submesoscale motions may be widely prevalent in the near-surface ocean. An observational strategy needs to be developed in order to ascertain the existence and nature of such motion. A better understanding of the phenomenon and its controlling parameters would be helpful; several questions still remain to be answered in this regard. For example: What determines the magnitude of the vertical velocities? Is the length scale of the submesoscale structures determinable from the linearized equations, or is it dependent on the nonlinear advective terms indicating the beginning of a forward energy cascade? Though the vertical motion discussed here is advective, it would generate large variations in lateral gradients and hence facilitate diapycnal mixing. Hence, we would like to ask what effect such motions might have on mixing and transport. Further, how does the submesoscale-mesoscale link affect the net vertical transport of nutrients and tracers? What are the cumulative rates of exchange that can be achieved between the surface and subsurface ocean through these features? Understanding the mechanism that underlies these motions is only the first step. It is of further interest to assess their implications and parameterize them.

Acknowledgements

We thank Leif Thomas for helpful suggestions and feedback, and James McWilliams and Baylor Fox-Kemper for insightful discussions. A.T. acknowledges support from NSF-OCE-0336786. A.M. acknowledges NOAA.

Appendix A. Model initialization

The model is set up in a west-to-east (W–E) periodic channel domain extending 48 km in the W–E (periodic) direction, 96 km in the south-to-north (S–N) direction, and centered at a latitude of 25°N. Impermeable vertical walls form the S and N boundaries of the domain and a flat bottom forms the lower boundary at 800 m. The domain is initialized with a sharp lateral S–N density gradient in the upper layers, such that the southern half of the domain has lighter water. This front, extending to a depth of 250 m, is representative of deep, semi-permanent fronts in the ocean. The vertical stratification is prescribed from a spline fit to an observed profile. The pycnocline, which is characterized by an approximate buoyancy frequency $N = 0.7 \times 10^{-2}\ \mathrm{s}^{-1}$, extends to about 250 m. It overlies a weakly stratified region and a nearly homogeneous deeper layer. A S–N density variation, $\Delta\rho$ is then superimposed on this vertical stratification. In the upper 50 m $\Delta\rho = 0.3\ \mathrm{kg\,m^{-3}}$, between 50 and 250 m $\Delta\rho = 0.3(250 - z)/200\ \mathrm{kg\,m^{-3}}$, where z is the depth in m, and below 250 m, there is no horizontal density variation. The density variation in the S–N direction is distributed according to $(\pm\Delta\rho/2)(1 - \exp(-y_c/2))/(1 + \exp(-y_c/2))$, where y_c is the distance in km from the center (Northward positive), and the ± signs are used according as y_c is positive or negative. The sea surface elevation is varied correspondingly over the same frontal region by 3.2 cm, being higher in the southern region. Associated with the S–N density front is an W–E geostrophic jet. The model velocities and nonhydrostatic pressure are initialized to be in geostrophic balance as described in Mahadevan (2006).

References

Bacastow, R., Maier-Reimer, E., 1991. Dissolved organic carbon in modeling oceanic new production. Global Biogeochemical Cycles 5, 71–86.

Bluestein, H.B., 1993. Synoptic-Dynamic Meteorology in Midlatitudes. Observations and Theory of Weather Systems, vol. 2. Oxford University Press, USA.

Capet, X., McWilliams, J.C., Molemaker, J., Shchepetkin, A., 2006. Mixed-layer instabilities in an upwelling system: Mechanisms and implications for the upper ocean dynamics. Eos Trans. AGU 87 (36), Ocean Sci. Meet. Suppl., Abstract OS23F-05.

Emerson, S., Quay, P., Karl, D., Winn, C., Tupas, L., Landry, M., 1997. Experimental determination of the organic carbon flux from open-ocean surface waters. Nature 389, 951–954.

Fox-Kemper, B., Ferrari, R., Hallberg, R.W., 2006. Modeling and parameterizing mixed layer eddies. Eos Trans. AGU 87 (36), Ocean Sci. Meet. Suppl., Abstract OS23F-06.

Garrett, C.J.R., Loder, J.W., 1981. Dynamical aspects of shallow sea fronts. Philosophical Transactions of the Royal Society of London Series A 302, 563–581.

Haynes, P.H., McIntyre, M.E., 1987. On the evolution of vorticity and potential vorticity in the presence of diabatic heating and frictional or other forces. Journal of the Atmospheric Sciences 44, 828–841.

Hoskins, B.J., Bretherton, Francis P., 1972. Atmospheric frontogenesis models: Mathematical formulation and solution. Journal of the Atmospheric Sciences 29 (6439), 11–37.

Hoskins, B.J., Draghici, I., Davies, H.C., 1978. A new look at the ω-equation. Quarterly Journal of the Royal Meteorological Society 104, 31–38.

Jenkins, W.J., 1988. Nitrate flux into the euphotic zone near Bermuda. Nature 331, 521–523.

Jenkins, W.J., Goldman, J.C., 1985. Seasonal oxygen cycling and primary production in the Sargasso Sea. Journal of Marine Research 43, 465–491.

Klein, P., Hua, B.L., 1988. Mesoscale heterogeneity of the wind-driven mixed layer: Influence of a quasigeostrophic flow. Journal of Marine Research 46, 495–525.

Lee, D., Niiler, P., Warn-Varnas, A., Piacsek, S., 1994. Wind-driven secondary circulation in ocean mesoscale. Journal of Marine Research 52, 371–396.

Levy, M., Klein, P., Treguier, A.-M., 2001. Impacts of sub-mesoscale physics on production and subduction of phytoplankton in an oligotrophic regime. Journal of Marine Research 59, 535–565.

Mahadevan, A., 2006. Modeling vertical motion at ocean fronts: Are nonhydrostatic effects relevant at submesoscales? Ocean Modelling 14 (3–4), 222–240.

Mahadevan, A., Archer, D., 2000. Modeling the impact of fronts and mesoscale circulation on the nutrient supply and biogeochemistry of the upper ocean. Journal of Geophysical Research 105 (C1), 1209–1225.

Maier-Reimer, E., 1993. Geochemical cycles in an ocean general circulation model. Global Biogeochemical Cycles 7, 645–678.

Martin, A.P., Pondaven, P., 2003. On estimates for the vertical nitrate flux due to eddy-pumping. Journal of Geophysical Research 108 (C11), 3359. doi:10.1029/2003JC001841.

McGillicuddy Jr., D.J., Robinson, A.R., 1997. Eddy induced nutrient supply and new production in the Sargasso Sea. Deep Sea Research, Part I 44 (8), 1427–1450.

McGillicuddy Jr., D.J., Robinson, A.R., Siegel, D.A., Jannasch, H.W., Johnson, R., Dickey, T.D., McNeil, J., Michaels, A.F., Knap, A.H., 1998. Influence of mesoscale eddies on new production in the Sargasso Sea. Nature 394, 263–266.

McWilliams, J.C., 2003. Diagnostic force balance and its limits Nonlinear Processes in Geophysical Fluid Dynamics. Kluwer Academic Publishers, pp. 287–304.

McWilliams, J.C., Molemaker, M.J., Yavneh, I., 2001. From stirring to mixing of momentum: Cascades from balanced flows to dissipation in the oceanic interior. Proceedings of the 12th ‘Aha Huliko’a Hawaiian Winter Workshop. SOEST, University of Hawaii, pp. 59–66.

McWilliams, J.C., Molemaker, M.J., Yavneh, I., 2004. Ageostrophic, anticyclonic instability of a geostrophic barotropic boundary current. Physics of fluids 16 (10), 3720–3725.

Molemaker, M.J., McWilliams, J.C., Yavneh, I., 2001. Instability and equilibration of centrifugally-stable stratified Taylor–Couette flow. Physical Review Letters 23, 5270–5273.

Molemaker, M.J., McWilliams, J.C., Yavneh, I., 2005. Baroclinic instability and loss of balance. Journal of Physical Oceanography 35 (9), 1505–1517.

Najjar, R.G., 1990. Simulations of the phosphorus and oxygen cycles in the world ocean using a general circulation model. Ph.D. thesis, Princeton University.

Najjar, R.G., Sarmiento, J.L., Toggweiler, J.R., 1992. Downward transport and fate of organic matter in the ocean: Simulations with a general circulation model. Global Biogeochemical Cycles 6, 45–76.

Niiler, P., 1965. On the Ekman divergence in an oceanic jet. Journal of Geophysical Research 74, 7048–7052.

Oschlies, A., 2002. Can eddies make ocean deserts bloom? Global Biogeochemical Cycles 16, 1106. doi:10.1029/2001GB001830.

Pedlosky, Joseph., 1987. Geophysical Fluid Dynamics, second ed. Springer-Verlag.

Pinot, J.-M., Tintore, J., Wang, D.-P., 1996. A study of the omega equation for diagnosing vertical motions at ocean fronts. Journal of Marine Research 54, 239–259.

Platt, Trevor., Harrison, William G., 1985. Biogenic fluxes of carbon and oxygen in the ocean. Nature 318, 55–58.

Pollard, R.T., Regier, L., 1990. Large variations in potential vorticity at small spatial scales in the upper ocean. Nature 348, 227–229.

Pollard, R.T., Regier, L.A., 1992. Vorticity and vertical circulation at an ocean front. Journal of Physical Oceanography 22, 609–625.

Rudnick, Daniel L., 1996. Intensive surveys of the Azores front. Part II: Inferring the geostrophic and vertical velocity fields. Journal of Geophysical Research 101 (C7), 16291–16303.

Shearman, R.K., Barth, J.M., Kosro, P.M., 1999. Diagnosis of three-dimensional circulation associated with mesoscale motion in the California current. Journal of Physical Oceanography 29, 651–670.

Stern, M.E., 1965. Interaction of a uniform wind stress with a geostrophic vortex. Deep Sea Research 12, 355–367.

Stone, P.H., 1970. On non-geostrophic baroclinic stability: Part II. Journal of the Atmospheric Sciences 27, 721–727.

Tandon, A., Zhao, L., 2004. Mixed layer transformation for the North Atlantic for 1990–2000. Journal of Geophysical Research 109. doi:10.1029/2003JC002059.

Thomas, L.N., 2005. Destruction of potential vorticity by winds. Journal of Physical Oceanography 35, 2457–2466.

Thomas, L.N., Lee, C.M., 2005. Intensification of ocean fronts by down-front winds. Journal of Physical Oceanography 35, 1086–1102.

Thomas, L.N., Rhines, P.B., 2002. Nonlinear stratified spin up. Journal of Fluid Mechanics 473, 211–244.

Thompson, L., 2000. Ekman layers and two-dimensional frontogenesis in the upper ocean. Journal of Geophysical Research 105, 6437–6451.

Ullman, D.S., Cornillon, P.C., 1999. Satellite-derived sea surface temperature fronts on the continental shelf of the northeast US coast. Journal of Geophysical Research 104 (C10), 23459–23478.

Viúdez, A., Dritschel, D.G., 2004. Potential vorticity and the quasigeostrophic and semigeostrophic mesoscale vertical velocity. Journal of Physical Oceanography 34, 865–887.

Voorhis, A.D., Bruce, J.G., 1982. Small-scale surface stirring and frontogenesis in the subtropical convergence of the western North Atlantic. Journal of Marine Research 40 (Suppl.), 801–821.